Dynamic Active Sites over Binary Oxide Catalysts: *In situ* /*Operando* Spectroscopic Study of Low-Temperature CO Oxidation over MnO_x-CeO_2 Catalysts

Xiao-man Zhang[a], *Ya-Qing Deng*[a], *Pengfei Tian*[a], *Huan-huan Shang*[a], *Jing Xu*[a] *and Yi-Fan Han*[a,b,]*

[a] State Key Laboratory of Chemical Engineering, East China University of Science and Technology, Shanghai 200237, China

[b] Research Center of Heterogeneous Catalysis and Engineering Sciences, School of Chemical Engineering and Energy, Zhengzhou University, Zhengzhou 450001, China

*E-mail: yifanhan@ecust.edu.cn.

Tel: +86-21-64251928. Fax:+86-21-64251928

Abstract

The determination of the dynamic active sites over binary oxide catalysts is of great challenge in heterogeneous catalysis. In this work, the origin of active sites toward low-temperature CO oxidation (<200 ^{o}C) were thoroughly studied using MnO_x-CeO_2 composite oxide catalysts with different Mn/Ce molar ration, synthesized by a redox co-participation method. The optimum Mn_1Ce_1 catalyst (T_{100} = 190 ^{o}C), which showed excellent activity, has found to be composed of three phases: (1) CeO_2; (2) amorphous MnO_x; (3) MnO_x-CeO_2 solid solution (active sites). With the combination of kinetics and characterization results, including Temperature-Programmed-Desorption/ Reduction (TPD/TPR), *operando* Raman spectroscopy and in situ diffuse reflectance infrared Fourier transform spectra (DRIFTS), the dynamic structures of catalysts were rationalized with the identification of the interface of MnO_x and CeO_2. The mechanism for CO oxidation over MnO_x-CeO_2 in the temperature range 100-190 ^{o}C were proposed that the direct and the formate routes were followed at T < 130 ^{o}C, and the carbonate route became dominant at T > 130 ^{o}C. Notably, the Mars-van Krevelen mechanism was proceeded in the whole temperature range. We speculate that cheap binary oxides will substitute for noble metal as catalysts for the removal of CO and other toxic gases, especially operating under mild conditions.

Keywords: dynamic structure; binary oxide; MnO_x-CeO_2; CO oxidation; *operando* spectroscopy

1. Introduction

Carbon monoxide (CO) at a certain level in air, as one of the most widely distributed atmospheric contaminants, endanger human's life [1]. The elimination of CO *via* catalytic oxidation of CO to CO_2 is still one of the most effective methods [2-4], either for industrial applications, indoor air purification and the treatment of exhaust gas from automobile. The well-known three-way catalysts for the latter mainly consist of noble metals (Pt, Rh, and Pd). However, due to its high cost, scarcity, sensitivity to sulphur poisoning, it is a great challenge to develop feasible catalysts, which should show excellent catalytic activity and thermal stability for practical application.

Ceria (CeO_2) has been widely applied as a surface modifier or a catalyst support for three-way catalysts [5-7], catalytic SO_x abatement [8] and low-temperature selectively catalytic reduction of NO_x (SCR) [9, 10]. The significance of CeO_2 for pollution abatement and other technologies are mainly due to: (1) the interaction with metal oxides to create active interfaces or boundaries [11]; (2) the low redox potential between Ce^{3+} and Ce^{4+} to charge the neighbor nanoparticles [12]; (3) the excellent oxygen-storage-capacity (OSC) to provide active oxygen species during reaction [13]; (4) the abundant oxygen vacancies in the surface to stabilize metal particles [11]. It is noted that the CeO_2 alone shows inferior activity due to slow oxygen-release and poor stability at elevated temperatures [14, 15]. Consequently, the Ce-based solid solutions formed by doping other cations into the CeO_2 lattice have proven superior

performances to the metal oxide alone, probably owning to doping-generated defects or new mixed oxide phases [16]. For instance, the rate for CO oxidation on CeO_2 was accelerated by 1-2 magnitudes by the combination with CuO and CeO_2 [17].

Manganese oxide (MnO_x: Mn^{2+}-Mn^{7+}) and its mixtures with the second metal oxide, such as MnO_x-CeO_2, MnO_x-ZrO_2 and MnO_x-TiO_2, have been studied as catalysts due to their high specific capacitance, environmental compatibility and non-toxicity [12, 18]. These catalysts were investigated for catalytic reactions such as CO oxidation, wet oxidation of phenol, decomposition of NO_x and VOC combustion [19, 20]. Ramesh et al. [21] has reported an activity order of CO oxidation as: MnO $<$ MnO_2 $<$ Mn_2O_3 below 250 °C. CO mainly reacted with the adsorbed O (O*) over Mn_2O_3 and MnO_2 catalysts, while the reaction of adsorbed CO (CO*) with the lattice oxygen (O_L) is primarily responsible for CO_2 formation on MnO. Han et al. [22] prepared Mn_3O_4 and Mn_2O_3 nanocrystals supported on mesoporous silica (SBA-15) using Mn (II and III) acetylacetonates as precursors. Both catalysts exhibited excellent stabilities and higher catalytic activities in comparison with MnO_x impregnated on SBA-15 catalysts. Xu et al. [23] has determined the near-surface structure of α-Mn_2O_3 nanocrystals by *operando* Raman spectroscopy (ORS) during the adsorption and oxidation of CO. With the combination of kinetics and vibrational information, they proposed that the mechanism for CO oxidation might shift from the Langmuir-Hinshelwood mechanism (<200 ^oC) to the Mars-van Krevelen mechanism (>350 ^oC) with varying the temperature. Among these MnO_x catalysts, MnO_2 exhibits several types of polymorphs, such as α-, β-, γ-, and δ-MnO_2. Their activities decreased

in the order of α- ≈ δ- > γ- > β-MnO_2. In addition, the Mn-O bond strength of MnO_2 can remarkably influence the activity [24].

The binary oxide catalysts, such as MnO_x-CeO_2, have been investigated for catalytic wet oxidation [25], VOC combustion [20], low-temperature SCR [26, 27], and preferential oxidation of CO [28, 29]. Qiao et al. [30] has prepared a series of mixed oxide catalysts, CeO_2-MO_x (M = Cu, Mn, Fe, Co, and Ni). The corresponding solid solution could be produced by the diffusion of metal ions into the CeO_2 lattice. Chen et al. [31] has synthesized $MnCeO_x$ in nanotube form with a specific surface area of 202 m^2/g, which can catalyze CO oxidation at ca. 200 ^oC. Zou et al. [32] reported that the catalytic activity toward CO oxidation showed a volcano curve with an increase in the Mn amount, while a $Mn_4Ce_6O_x$ sample with a surface area of 215 m^2/g has found the highest activity. All experimental results have proven that the activity of binary MnO_x-CeO_2 is better than the CeO_2 or MnO_x alone. In accordance with the previous studies, the active oxygen species on the interfaces between MnO_x and CeO_2 play an important role in CO oxidation [32, 33]. However, it notes that the reaction mechanism involving the surface intermediates of CO oxidation over MnO_x-CeO_2 catalysts is still very rare in the open literature. Several questions about this catalytic system are still ambiguous. For instance, what is the actual role of interface between MnO_x and CeO_2 in the whole reaction process? How do MnO_x and CeO_2 interact during activation and reaction processes? Such a study may extend to the elucidation of the dynamic active structure of other binary oxide catalysts.

In this study, in order to improve the texture structure, the morphological properties, and the redox behavior of the catalysts, MnO_x-CeO_2 composite oxides are synthesized by a redox co-precipitation method. For the determination of the evolution of active sites during the processes of activation and reaction, the catalytic performance and structure characterization are performed using multi-techniques, including in situ/Operando Raman spectroscopies. Ultimately, the plausible mechanism was rationalized.

2. Experimental

2.1. Catalyst preparation

MnO_x-CeO_2 catalysts with different Mn/Ce mole ratios (0.33-2) were prepared by a redox co-precipitation method [34]. The $KMnO_4$ precursor dissolved in deionized water, in a 10% stoichiometric excess, was titrated with a solution of $Ce(NO_3)_3$ and $Mn(NO_3)_2$ at 60 ^oC under vigorous stirring, keeping pH=8.0 ± 0.3 using a 0.2 M KOH solution. After titration, the solid was digested for 30 min at 60 ^oC and then filtered, repeatedly washed with hot distilled water, and dried overnight at 100 ^oC. Aliquots of the dried samples were further calcined in air at 400 ^oC (6 h). N_2 adsorption and desorption isotherms were collected on an Autosorb-6 at -198 ^oC.

2.2. Catalytic evaluation

The activity of the catalysts for CO oxidation was carried out using a micro fixed-bed reactor, in which a quartz tube with ID 4 mm was located in a ceramic tube

oven under differential conditions with the catalyst powder of 50.0 mg (catalyst bed length: 5-8 mm) in a gas mixture of 1%CO/20%O_2/Ar. Influent and effluent gases were analyzed with an online gas chromatograph (Shanghai Ruimin, Model GC2060) equipped with a CP-carbon BOND column. The CO conversions were calculated according to Eq.(1):

$$\text{CO conversion } (\%) = n_{CO_2,out}/(n_{CO_2,out} + n_{CO,out}) \times 100 \quad (1)$$

where $n_{CO,out}$ and $n_{CO_2,out}$ are the corresponding GC response peak area values of CO and CO_2, respectively.

2.3. Characterization

Operando Raman spectra (ORS) were measured with an *operando* setup using a Raman microscope (LabRAM HR, Horiba J.Y.), a detail description of this system was already given in ref. [35]. The temperature ramping rate was 10 ^{o}C/min when the sample was heated from 25 to 500 ^{o}C. The exhaust gas was analyzed using a GC-QMS (HPR-20, Hiden Analytical Ltd.).

Scanning Electron Microscope (SEM) was performed on a JEOL JSM-6700F field emission SEM, which was operated at the accelerating voltage of 15 kV and the detector current of 10 mA. Transmission electron microscopy (TEM) was conducted on a JEOL JEM 2100 microscope operated at 100 kV.

X-ray diffraction (XRD) patterns were obtained with a Bruker D8 diffractometer using Cu Kα radiation (λ = 1.540589 Å). The crystal size of samples was calculated

from the width of diffraction profiles, referring to the full width at half maximum (FWHM) of the crystalline phase using the Debye-Scherrer formula.

Temperature-programed desorption/reduction (TPD/TPR) experiments were performed using a micro fixed-bed reactor (a quartz reactor 20 cm long and 0.4 cm in diameter) connected to a GC-QMS (HPR-20, Hiden Analytical Ltd.), where masses (m/e: 18(H_2O), 28(CO), 32(O_2), 44(CO_2)) were monitored. All TPD experiments started with as-prepared MnO_x-CeO_2 catalyst. The catalyst was purged with Ar (50 ml/min) for 1 h at 250 ^oC. After pretreatment, the sample was exposed to 20%O_2/Ar or 1%CO/Ar with a flow of 50 mL·min^{-1} at 30 ^oC for 1 h. Following a purge with Ar until a stable baseline was obtained. The temperature ramping rate was 20 ^oC·min^{-1} in an Ar flow of 50 ml/min from 30 ^oC to 850 ^oC.

With pretreating the samples following the same procedure as abovementioned, TPR was performed in a temperature range 30-850 ^oC with a rate of 10 ^oC min^{-1} in a 10% CO/Ar flow (50 ml/min). The process of H_2-TPR was in accordance with that of CO-TPR.

In situ Diffusion reflectance infrared Fourier transform (DRIFT) spectra were recorded using a Fourier transform infrared spectrometer (Perkin-Elmer, Model Spectrum 100) with a mercury-cadmium-tellurium (MCT) detector and an in situ cell (modified Harricks Model HV-DR2), with a resolution of 4 cm^{-1}. An accumulation of 100 scans was used for collecting the spectra. About 50 mg of the catalyst was placed in the cell and pre-treated at 250 ^oC for 1 h in a flow of Ar (30 ml min^{-1}) to remove

water in the catalyst. Subsequently, the system was cooled down to 20 ^{o}C and the background spectrum was recorded. Spectra were obtained for catalysts in a stream of 1.0% CO, balance Ar and 1.0% CO, 20% O_2, balance Ar with a total flow rate of 50 ml/min, and a ramping rate of 1 ^{o}C min^{-1}.

3. Results and discussion

3.1. Catalyst structure

The XRD patterns (Fig. 1) displays MnO_x-CeO_2 with different molar ratios, while pure CeO_2 was used as a reference (spectrum G). The diffraction peaks at 28.5°, 33.1°, 47.5°, 56.4° and 59.1° were assigned to plane facets (111), (200), (220), (311) and (222) (JCPDS 89-8436), respectively. The diffraction peaks of MnO_x at 28.7°, 37.5°, 42.9°, 56.8° and 23.8°, 27.2° were assigned to the plane facets (110), (101), (111), (211) (JCPDS 72-1984) for MnO_2 and the plane facets ($\bar{1}$22), (210) (JCPDS 79-0083) for Mn_2O_7. $Mn_{0.33}Ce_1$ catalyst only shows characteristic diffraction peaks of CeO_2 at 28.6°, 33.0°, 47.5°, 56.3°, which slightly shift comparing with CeO_2, while the peaks corresponding to MnO_x were not determined. The absence of diffraction peaks of manganese oxides implies that there exist two kinds of Mn species in the samples: Mn ions incorporated into the ceria lattice and highly dispersed MnO_x on the surface of ceria [36]. Additionally, the slight shift of the diffraction peaks of these samples to higher Bragg angles was due to incorporation of smaller size of Mn ions (Mn^{2+} = 0.083 nm, Mn^{3+} = 0.065 nm, Mn^{4+} = 0.053 nm) into the ceria lattice. Peak shift and the absence of diffraction peaks of MnO_x confirm the formation of MnCe solid

solutions [37]. The peaks for CeO_2 become broad with an increase in the Mn concentration, indicating the decrease in the crystal size of catalysts.

The particle sizes and surface area of all MnO_x-CeO_2 catalysts are listed in Table 1. The morphology of Mn_1Ce_1 (Fig. 2a) and the lattice spacing (Fig. 2b), d_{111} = 0.31 nm and d_{200} = 0.27 nm for CeO_2, were observed from the HRTEM images. Moreover, the lattice fringe of MnO_x was not observed, probably because of the generation of the MnO_x-CeO_2 solid solution by incorporation of Mn^{n+} into the CeO_2 lattice. This could also be demonstrated by the SEM-EDX spectra (Fig. 3), while Mn and Ce elements were distributed uniformly.

3.2. Activity

CO oxidation was recorded in a stream of 1.0 kPa CO, 20.0 kPa O_2 (rest Ar) over MnO_x-CeO_2 catalysts (Fig. 4a). On the basis of 10% conversion of CO, T_{10} = 290 ^oC, the CeO_2 alone exhibited the lowest activity; CO conversion was still less than 40% at 350 ^oC. T_{10} = 120 ^oC was observed for the MnO_x alone, being superior to CeO_2, a complete conversion of CO was observed at 260 ^oC. With the addition of Mn, the activity for MnO_x-CeO_2 catalysts increased from MnO_x (T_{10} = 120 ^oC) to Mn_1Ce_1 (T_{10} = 66 ^oC), and then dropped down over $Mn_{1.5}Ce_1$. An activity order for all catalysts was followed as: CeO_2 < MnO_x ≈ $Mn_{0.33}Ce_1$ < $Mn_{0.75}Ce_1$ < Mn_2Ce_1 < $Mn_{1.5}Ce_1$ < Mn_1Ce_1. Interestingly, this tendency is line with the change in the catalyst surface area. Among all catalysts, the Mn_1Ce_1 catalyst showed the highest activity with T_{10} at 66 ^oC and T_{100} at 190 ^oC. Apparently, the Mn_1Ce_1 catalyst exhibited higher catalytic activity

and broader temperature window for CO conversion. The activity for CO oxidation over various MnO_x-CeO_2 catalysts was summarized in Table 2.

Moreover, by a comparative study in the temperature range 50-400 ^oC (Fig. 4b and 4c) to study the effect of moisture, we found that the CO oxidation activity over Mn_1Ce_1 catalyst significantly declined in the presence of 1.5 vol% water (Fig. 4b). The light-off temperature T_{10} was 110 ^oC, while the T_{100} reached to 320 ^oC compared with T_{100} = 190 ^oC under the water-free condition. But when it was switched to a water-free atmosphere during the cooling procedure after an Ar flow purged, there was an improvement of the activity (T_{100} = 200 ^oC), which was consistent with the activity in the absent of water. The adsorbed water on the catalyst surface is supposed to partially occupy the active sites for CO oxidation, leading to the decrease of the active sites and the decline of the activity. While, the introduction of water didn't change the structure of the catalyst, so, after purging with Ar the activity could be restored reversibly. Our results could be confirmed by previous studies [38, 39].

3.3. Temperature-programmed experiments

H_2-TPR (Fig. 5a) was performed to investigate the redox property of the MnO_x-CeO_2 catalysts. Only one reduction peak at 490 ^oC was detected for CeO_2, being attributed to the reduction of the surface oxygen [11]. An asymmetrical peak at 317 ^oC was observed for MnO_x, due to a stepwise reduction of $Mn^{4+} \rightarrow Mn^{3+} \rightarrow Mn^{2+}$ [40]. For MnO_x-CeO_2 catalysts, only one reduction peak at 262 ^oC was observed for Mn/Ce ratio less than 0.75, probably resulting from the formation of the homogeneous

phase (solid solution) between MnO_x and CeO_2, while two reduction peaks at 246 ^oC and 282 ^oC were detected for Mn/Ce ratio larger than 1. Accordingly, the low temperature peak could be attributed to the reduction of highly dispersed surface manganese species (MnO_2/Mn_2O_3) to Mn_3O_4 and the peak at high temperature was assigned to the reduction of Mn_3O_4 to MnO together with the reduction of surface ceria [41]. With the addition of Mn, the first peak shifted down from 270 ^oC on $Mn_{0.33}Ce_1$ to 246 ^oC on Mn_1Ce_1. With continuously increasing the Mn/Ce ratio to 1, the second peak at 282 ^oC was observed and its intensity increases proportionally with the content of Mn. In comparison with CeO_2 and MnO_x, the decrease in the reduction temperature could be associated to the synergistic interaction between Mn-O and Ce-O, which led to the formation of MnO_x-CeO_2 solid solution. The mobility of oxygen species from the bulk to the surface in the solid solution was greatly enhanced, thereby creating more active sites on the surface for the adsorption of oxygen [42]. As listed in Table 1, Mn_2Ce_1 showed the largest H_2-consumption (0.15 mmol/g), which may indicate the formation of mixture of MnO_x and MnO_x-CeO_2 with the excess of MnO_x.

O_2-TPD (Fig. 5b) was performed to investigate the adsorbed oxygen species. A distinct desorption peak at 470 ^oC can be ascribed to the O_L for pure CeO_2 (spectrum G). Two inconspicuous desorption peaks at 300 ^oC and 800 ^oC are assigned as the surface and bulk O_L from MnO_x (spectrum A), respectively. There is only one symmetrical desorption peak at 450 ^oC for $Mn_{0.33}Ce_1$; with further increasing the content of Mn, two desorption peaks appeared at 424-489 ^oC and 597-621 ^oC,

corresponding to the O_L on the near-surface region of the catalyst. The O_2-storage capacity (OSC) of MnO_x-CeO_2 catalysts was also outlined in Table 1. The amount of O_2-storage increased initially but deceased with further addition of Mn after surpassing a maximum of 0.22 mmol/g for Mn_1Ce_1.

On the basis of H_2-TPR and O_2-TPD profiles, we conclude the existence of three phases in Mn_1Ce_1: (1) CeO_2; (2) amorphous MnO_x; (3) MnO_x-CeO_2 solid solution (active sites). As displayed in Fig. 4a, Mn_1Ce_1 with the largest OSC and the lowest H_2 reduction temperature showed the highest activity, we deduce there is an abundant active oxygen species on the surface. In comparison with the inferior activity for pure CeO_2 and MnO_x, the interaction between MnO_x and CeO_2 obviously enhanced the redox property of MnO_x-CeO_2.

The strong interaction between MnO_x and CeO_2 could promote the transfer of electron from O to Mn ions (e.g., O^{2-}-$Mn^{4+} \rightarrow O^{-}$-$Mn^{3+}$), resulting in the formation of active electrophilic oxygen species and enhancement of the surface oxygen mobility [43]. The addition of Mn could also facilitate the reducibility of CeO_2 and boost the formation of superoxo (O_2^-) and/or peroxo species (O_2^{2-}) from adsorbed O_2 [44]. The density functional theory calculations also demonstrated that the doping of Mn induced the formation of structural O-vacancies in the CeO_2 lattice [45]. The charge redistribution occurred upon the creation of the MnO_x-CeO_2 surface, where Mn (Mn^{3+}) acts as an electrons acceptor, lowering the energy for the creation of oxygen vacancy at the rim of the dopant and greatly promoting the activation of adsorbed molecular

oxygen.

It has been reported that the MnO_x-CeO_2 solid solution in the catalyst was responsible for its excellent activity [42, 46]. The redox couple (Mn^{4+}→Mn^{3+}→Mn^{2+} and Ce^{3+}→Ce^{4+}) in the solid solution made the surface O_L on MnO_x-CeO_2 much easier to be activated than that on the MnO_x or CeO_2 alone; We assume more surface active oxygen species are generated during reaction. It is clear that the low light-off temperatures for MnO_x-CeO_2 catalysts should be due to the synergetic effect of Ce and Mn species, which leads to (i) the higher specific surface area and smaller crystal size of the MnO_x-CeO_2 catalysts, (ii) the abundant number of surface oxygen species, and (iii) the improved surface redox property as identified by H_2-TPR.

CO-TPR profiles (Fig. 6) were employed to evidence the reducible surface oxygen species for CeO_2, MnO_x and Mn_1Ce_1 catalysts. Three regions of (I) 255-400 ^oC, (II) 400-557 ^oC and (III) 557-668 ^oC were distinguished for CeO_2 (Fig. 6a). In region (I), the dropdown of CO with uprising of CO_2 indicates the O_L in CeO_2 migrates and reacts with CO_{ad} to generate CO_2. In region (II), the CO consumption and the CO_2 generation reached a steady state. In region (III), the release amount of oxygen was reduced, leading to a decrease in CO consumption until the exhaust of the O_L. It is noted that CO could be oxidized into CO_2 without gaseous O_2 in the whole range. In addition, the H_2O signal emerged at above 110 ^oC, probably resulting from the combination of surface hydroxyl and oxygen. Therefore, CO-TPR also could be conducted to probe the activation of surface hydroxyls to produce water.

CO-TPR profiles for MnO_x (Fig. 6b) revealed that the surface oxygen on MnO_x and Mn^{3+}-O were activated and reacted with CO to form CO_2 at ca. 100 ^oC. Then, the O_L in the bulk and Mn^{4+}-O started to be released after the surface oxygen had been run out completely at above 416 ^oC. In comparison with CeO_2, MnO_x has much more O_L in bulk than that on the surface and subsurface, so that O_L could not be consumed completely by CO at the end of the reduction. The CO-TPR profile for Mn_1Ce_1 (Fig. 6c) is similar to CeO_2, but a broad desorption peak (140-850 ^oC) for H_2O was detected, indicating the existence of abundance of surface hydroxyl. From the O_2-TPD of Mn_1Ce_1, we observed that O_L started to be released at 225 ^oC, which was lower than MnO_x (295 ^oC) and CeO_2 (465 ^oC). We assume that the redox couples ($Mn^{4+}\rightarrow Mn^{3+}\rightarrow Mn^{2+}$ and $Ce^{3+}\rightarrow Ce^{4+}$) in the solid solution allow the surface O_L on MnO_x-CeO_2 much easier to be activated than that from MnO_x and CeO_2. Hence, the enhancement of oxygen mobility could supply more surface active oxygen species under the reduction condition, which plays the decisive role for CO oxidation.

3.4. Operando Raman spectroscopy

In order to determine the dynamic structure of the catalyst during CO adsorption and oxidation, real-time Raman spectra over bulk CeO_2 and MnO_x-CeO_2 catalysts were recorded under reaction conditions. The Raman signal of CeO_2 (Fig. 7) is dominated by the strong F_{2g} mode of CeO_2 fluorite phase at 465 cm^{-1} [47], which is the symmetric vibration of oxygen with adjacent cations. This mode is sensitive to the disorder of surface O_L and the change in catalyst particle size. Several weak bands at

1050, 582 and 255 cm^{-1} can be assigned to the second-order longitudinal optical (2LO) mode, oxygen vacancy and second-order transverse acoustic (2TA) mode, respectively. The 2LO mode is caused by the phonon relaxation from the resonance Raman effect [48]. In the flow of Ar (Fig. 7a) and CO (Fig. 7b), the spectra are quite stable in 25-500 ^{o}C. Under the reaction conditions (Fig. 7c), the peaks downshifted to a lower wavenumber with temperature. The red-shift of the F_{2g} mode and its asymmetric broadening can be very well explained by inhomogenous strain effects associated with the dispersion of particle size using the phonon confinement model and the presence of oxygen vacancies [49].

The Raman spectra for Mn_1Ce_1 in Ar (Fig. 7d) show the bands at 350 cm^{-1}, 564 cm^{-1} and 636 cm^{-1}, which are attributed to the out-of-plane bending modes of MnO_x, asymmetric stretching of bridge oxygen species (Mn-O-Mn), and the symmetric stretch of Mn-O_x groups, respectively [23]. With referring pure CeO_2, the main peak, the F_{2g} mode of CeO_2 shifted down from 465 cm^{-1} to 447 cm^{-1} because of the formation of the MnO_x-CeO_2 solid solution. The shift of F_{2g} band also indicates that the interaction between Mn and Ce deformed the fluorite-like structure and resulted in the formation of the oxygen vacancies in the CeO_2 lattice [50]. The peak for the F_{2g} mode of CeO_2 at 447 cm^{-1} increased significantly, while the peak at 636 cm^{-1} for MnO_x shifted to 603 cm^{-1} at above 300 ^{o}C. It may be due to the desorption of surface active oxygen species and the formation of oxygen vacancies. This result agrees well with O_2-TPD profiles, indicating the release of O_L at 300 ^{o}C. The theoretical calculations also demonstrated that, on the oxygen vacancies of CeO_2 near the Mn

dopant, O_2 molecules were facile to be adsorbed and then charged by the Mn-O state to form superoxo (O_2^-) and/or peroxo species (O_2^{2-}) due to the strong interaction between MnO_x and CeO_2 [44]. The intensity of F_{2g} peak increased with temperature, indicating that the lattice parameter of MnO_x-CeO_2 was altered during the heating [51]. Similar Raman spectrum appeared again (spectrum A in Fig. 7b) when the temperature decreased to room temperature (Fig. 7d). This phenomenon suggests that the surface O_L can be constantly replenished, owing to the migration of the bulk O_L toward the surface region. In comparison with the Raman spectrum measured under Ar, the peak intensity at 642 cm^{-1} measured in 1% CO/Ar (Fig. 7e) decreased at 300 ^oC, and vanished completely at 400 ^oC. This may be induced by a phase transformation of MnO_x, due to a loss of O_L. However, the band at 636 cm^{-1} appeared again when returning to room temperature, with a slight upshift to 642 cm^{-1}, which indicated that the near/sub-surface structural modification for Mn_1Ce_1 by CO was also reversible. The *operando* Raman spectra (Fig. 7f) showed that four Raman peaks remained unchanged until 400 ^oC. The intensity of peaks at 564 cm^{-1} and 643 cm^{-1} increased with temperature, probably caused by the lattice expansion [52]. On the other hand, *Operando* spectroscopy also suggests that the surface O_L reacted with CO can be continuously compensated by gaseous O_2 following the redox mechanism.

3.5. In situ DRIFTS

CO-DRIFTS were recorded for CeO_2 in a stream of CO (Fig. 8a) with increasing the temperature from 25 to 500 ^oC. Two peaks at 2170 cm^{-1} and 2123 cm^{-1} appearing

at 25 ^{o}C could result from gaseous CO, while no peak of adsorbed CO was observed below 300 ^{o}C. A new feature at 2170 cm^{-1} was detected at above 300 ^{o}C, probably associating with the linearly adsorbed CO on Ce^{4+} [53]. The peak intensity at 2170 cm^{-1} increased proportionally with temperature. In the meantime, three characteristic peaks at 1268, 1236, 1068 cm^{-1} were detected, originating from the carbonate and carboxylate species [54]. A small peak at 1370 cm^{-1} could be raised from the formate species. In addition, the intermediates, including carbonates and carboxylate species, also increased with temperature. In the meantime, more Ce^{4+} sites are likely generated with temperature, leading to a rise in the intensity of linear CO-Ce^{4+}. The CO-TPR profiles have also proven that the creation of oxygen vacancies due to the depletion of the surface O_L of CeO_2

Two peaks at 3658 and 3555 cm^{-1} could be attributed to isolated hydroxyl groups [53]. The reverse peak around 3555 cm^{-1} became more intensive with temperature, indicating the reduction of OH groups. Thus is responsible for the drop in band intensities of the formate species. It also indicates that the OH groups react with CO to form the formate species even at low temperatures; meanwhile, the adsorption of CO on CeO_2 was suppressed in the presence of surface OH species.

In addition, an increase in the intensity of intermediates with temperature, including carbonate and carboxylate species, is an indicative of the enhancement of the reaction rate between CO and the surface O_L or surface OH groups. Li et al. [54] has reported the thermal stability order of these species in different adsorption modes

as: bridged carbonate < bidentate carbonate < inorganic carboxylate < unidentate carbonate species. Among them, unidentate carbonate species are rather stable up to 500 ^{o}C. In addition, the bidentate carbonate species can be converted into unidentate carbonate (1068 cm^{-1}) at high temperatures [54, 55].

Then, DRIFTS spectra of CeO_2 (Fig. 8b) were recorded in a stream of 1.0 kPa CO and 20 kPa O_2 in Ar following the same process. Similar to those in the O_2-free atmosphere, gaseous CO at 2170 and 2123 cm^{-1} was observed, while no peak for CO adsorption was observed during the heating process. Up to 300 ^{o}C, the irregular peaks at 2300-2400 cm^{-1}, corresponding to gaseous CO_2, grew continuously with temperature. Meanwhile, the intensity of OH groups (3658 and 3555 cm^{-1}) decreased gradually, and the intensity of carbonate and carboxylate species (1268, 1233 and 1070 cm^{-1}) and formate species (1367 cm^{-1}) increased simultaneously. It is consistent with the tendency of activity (Fig. 4) that CO oxidation started at 300 ^{o}C (T_{10}=291 ^{o}C).

In situ DRIFTS on MnO_x in 1% CO/Ar (Fig. 9a) also revealed that gaseous CO could be detected during the activation process. The peaks at 1494, 1418 and 1360 cm^{-1} can be assigned to the carbonate species, the intensities of which increased with temperature, reflecting that CO reacted with the active surface O_L of MnO_x to produce the carbonate species. The peak at 3345 cm^{-1}, assigned to OH groups, decreased with temperature by forming formate species.

Subsequently, in situ DRIFTS spectra for MnO_x were recorded under reaction

conditions (Fig. 9b). The characteristic peaks of gaseous CO were only observed below 250 ^{o}C; the peaks for gaseous CO_2 then emerged at above 250 ^{o}C with an increase in their intensities simultaneously. The peaks at 1670, 1568 and 1340 cm^{-1} at 25 ^{o}C could also be assigned to the formate species, which are different with those in 1%CO/Ar, probably because of the participation of O_2. The intensity of formate species decreased and completely vanished at 200 ^{o}C. It hints that the formate species were easily decomposed by thermolysis [53].

Finally, under the same conditions, in situ DRIFTS spectra of MnO_x-CeO_2 were recorded in a feed gas of 1.0 kPa CO and Ar balance (Fig. 10a). Similar to CeO_2, the OH groups centered at 3656 cm^{-1} became more intensive with the increase of temperature, which could be responsible to the reduction of formate species. At 150 ^{o}C, a new peak at 2228 cm^{-1} appeared, being assigned to linearly adsorbed Mn^{2+}-CO [56]. The peak intensity increased proportionally in 25-150 ^{o}C, but completely fade away at 250 ^{o}C. The characteristic peaks, carbonate and carboxylate at 1614, 1533, 1470, 1394 and 1218 cm^{-1} and formate species at 1568 and 1348 cm^{-1}, suggest that CO can react with the surface active O_L and OH groups of MnO_x-CeO_2 to form these species at low temperatures, and the exposed metal ions Mn^{n+} could play as adsorption sites for CO. The peaks of carbonate, carboxylate and formate species increased with temperature because their generation rates were faster than the decomposition rate in the oxygen-free atmosphere.

Distinct CO_2 peaks for Mn_1Ce_1 appeared at 100 ^{o}C under the reaction conditions

(Fig. 10b) and grew continuously with temperature, accompanied with the gradual disappearance of the gaseous CO peaks until 100% conversion of CO at 250 ^{o}C; it is coincided with the temperature-dependent CO conversion (T_{100}=190 ^{o}C). The drop in carbonate species with temperature indicates its generation rate is lower than its decomposition rate during the heating process; the carbonate species inclined to decompose into CO_2 in the presence of oxygen. There was no linear adsorption peak for CeO_2 because the catalyst surface was dominated by the mixture of MnO_x-CeO_2, which agreed well with previous hypothesis [37]. The decomposition of the carbonate species created defects as well, such as oxygen vacancies and Ce^{3+} ions [57]. The oxygen vacancies in the interface between MnO_x and CeO_2 first captured the gas-phase oxygen, and then formed active interface oxygen species, such as O_2^-. This kind of active interface oxygen could be easily extracted by CO to form CO_2 via the intermediates of bidentate carbonates [32]. Finally, O_L was replenished by gaseous oxygen.

3.6. Mechanism of CO oxidation over MnO_x-CeO_2 catalysts

Kinetic measurements were performed over Mn_1Ce_1. Dependence of reaction rate on the partial pressure of CO and the partial pressure of O_2 could be seen in Fig.S1. The reaction order with respect to CO (α_{CO}) rose from 0.3 to 0.8 with increasing the temperature, the reaction order with respect to O_2 (α_{O_2}) decreased from 0.3 to 0.1, and remained with further increasing the temperature. Thus, we infer that CO should first be adsorbed by creating an unstable intermediate with O_L, which is further

decomposed into CO_2. In short, the reaction should proceed *via* the Mars-van Krevelen mechanism. Temperature-dependent rates were plotted with an Arrhenius diagram (Fig. S2). The calculated activation energy was equal to 29 ± 1.7 kJ/mol. All kinetic parameters, including reaction orders and apparent activation energy, were listed in Table 3. In comparison with manganese oxide and manganese-cerium oxide catalysts in other references, the E_a value was reduced by ca.30-40 kJ/mol for Mn_1Ce_1 in the present study.

Zou et al. proposed the CO oxidation reaction pathway over Mn-Ce catalysts which involved the bidentate carbonates as reaction intermediates [32]: the oxygen vacancy on the interface between MnO_x and CeO_2 captures the gas-phase oxygen, forming active interface oxygen species which can be easily extracted by CO to form CO_2 via the intermediates of bidentate carbonates. However, more reaction intermediates were observed in the present study and the reaction undergoes different pathways at various temperature ranges. With the combination of kinetic data and *operando*/in situ spectroscopies, and based on many previous work, the mechanism of CO oxidation over MnO_x-CeO_2 catalyst is depicted in Scheme 1. We propose:

(i) In the temperature range of 100-130 ^oC, two parallel pathways are responsible for CO oxidation: (1) the CO adsorbed on metal ions reacts with the adjacent lattice oxygen (O_L) to form CO_2, and then generates oxygen vacancies (O_V), which has already been evidenced by *operando* Raman spectroscopy (Fig. 7).

$$O_L + CO \rightarrow CO_2 + O_V \quad (2)$$

Due to the incorporation of Mn^{n+} into the CeO_2 lattice, there are two redox couples, $Mn^{4+}\rightarrow Mn^{3+}\rightarrow Mn^{2+}$ and $Ce^{4+}\rightarrow Ce^{3+}$, leading to its excellent redox property. The CO-TPR profile demonstrates the surface oxygen is feasible to be activated in the presence of CO. New oxygen vacancies could be formed after CO reacting with the surface O_L. Three kinds of surface oxygen vacancies in fluorite structure catalysts have been observed by Scanning Tunneling Microscope (STM) image: single surface vacancy; linear surface oxygen vacancies; surface oxygen vacancy trimers [51]. Single surface vacancy is produced by removal of the surface O_L, then the adjacent O atoms are activated immediately to form linear surface oxygen vacancies, and finally the most stable structure, which is a trimer consisting of two surface oxygen vacancies and one subsurface oxygen vacancy, can be generated. The taking-off temperature for CO oxidation, or to say, the catalytic activity, is mainly decided by the activation of the surface O_L.

(2) CO is oxidized through the formate route. As a certain amount of OH groups are present on the catalyst surface, adsorbed CO on Ce reacts with the adjacent O from OH to form the formate intermediate (HCOO*), which further decomposes into CO_2. In addition, the generated H atoms react with surface hydroxyl to form H_2O.

(ii) At above 130 ^{o}C, CO oxidation occurs through the formation of carbonate. In O_2 atmosphere, the O_V sites will be first occupied by dioxygen *via* bonding to Mn and Ce ions, forming two activated surface O_L (active O_L) (Scheme 1). Then carbonate intermediates (CO_3*) are formed by the combination of adsorbed CO with active O_L,

being easily decomposed into CO_2 at higher temperatures. Once CO_2 is desorbed from the surface, the original structure of MnO_x-CeO_2 surface will be recovered. In general, the Mars-van Krevelen mechanism should be responsible for this reaction in the whole temperature range.

By the Operando/in situ spectroscopies, for this first time, the dynamic structure of binary oxide catalyst, MnOx-CeO_2, was systematically characterized during the activation and reaction processes. In combination with kinetics, the plausible mechanism for CO oxidation on MnO_x-CeO_2 was rationalized. We believe that insights and research methods derived from this study can be extended to other oxide catalysts and similar reactions.

4. Conclusions

The dynamic structures of MnO_x-CeO_2 catalysts during reaction were characterized using in situ/*operando* spectroscopy. The catalytic active sites towards CO oxidation and kinetics in the low-temperature region were also investigated. We conclude:

(i) MnO_x-CeO_2 composite is composed of three phases: CeO_2, amorphous MnO_x and MnO_x-CeO_2 solid solution. CeO_2 could be an oxygen-storage reservoir to supply the surface O_L, which is identified as the main active species of MnO_x-CeO_2.

(ii) An activity order of CeO_2 < MnO_x ≈ $Mn_{0.33}Ce_1$ < $Mn_{0.75}Ce_1$ < Mn_2Ce_1 < $Mn_{1.5}Ce_1$ < Mn_1Ce_1 was observed. Among all catalysts, Mn_1Ce_1 exhibited the highest

activity (T_{10} = 70 ^{o}C, T_{100} = 190 ^{o}C), which was attributed to the strong interaction between MnO_x and CeO_2.

(iii) We assume that the mechanism for CO oxidation over MnO_x-CeO_2 may change with temperature. At 100-130 ^{o}C, the reaction may proceed through two parallel routes: (1) CO reacts with the surface O_L directly to generate oxygen vacancies (the direct route); (2) CO reacts with the adjacent O from surface OH to generate formate as an intermediate (HCOO*), which could decompose into CO_2 (the formate route). At above 130 ^{o}C, the reaction goes through the carbonate route. The adsorbed CO at oxygen vacancies reacts with the surface O_L to generate carbonate species, which could decompose into CO_2 in the presence of O_2. Notably, the Mars-van Krevelen mechanism is followed in the whole temperature range.

Acknowledgements

The authors are grateful to the support from the National Science Foundation (91534127, U1463205, 21273070 and 21576084), the Program for New Century Excellent Talents in university (NCET-12-0852), and the Chinese Education Ministry 111 project (B08021).

References

[1] A. Ernst, J.D. Zibrak, New Engl. J. Med. 339 (1998) 1603-1608.

[2] M.S. Chen, Y. Cai, Z. Yan, K.K. Gath, S. Axnanda, D.W. Goodman, Surf. Sci. 601 (2007) 5326-5331.

[3] B.K. Min, C.M. Friend, Chem. Rev. 107 (2007) 2709-2724.

[4] H.-J. Freund, G. Meijer, M. Scheffler, R. Schlögl, M. Wolf, Angew. Chem. Int. Ed. 50 (2011) 10064-10094.

[5] J.C. Summers, S.A. Ausen, J. Catal. 58 (1979) 131-143.

[6] G. Kim, Ind. Eng. Chem. Prod. Res. Dev. 21 (1982) 267-274.

[7] J. Kašpar, P. Fornasiero, M. Graziani, Catal. Today 50 (1999) 285-298.

[8] A.A. Bhattacharyya, G.M. Woltermann, J.S. Yoo, J.A. Karch, W.E. Cormier, Ind. Eng. Chem. Res. 27 (1988) 1356-1360.

[9] R. Jin, Y. Liu, Z. Wu, H. Wang, T. Gu, Chemosphere 78 (2010) 1160-1166.

[10] B. Shen, X. Zhang, H. Ma, Y. Yao, T. Liu, J. Environ. Sci. 25 (2013) 791-800.

[11] A. Trovarelli, Catal. Rev. 38 (1996) 439-520.

[12] B. Murugan, A.V. Ramaswamy, D. Srinivas, C.S. Gopinath, V. Ramaswamy, Chem. Mater. 17 (2005) 3983-3993.

[13] X. Yao, C. Tang, Z. Ji, Y. Dai, Y. Cao, F. Gao, L. Dong, Y. Chen, Catal. Sci. Technol. 3 (2013) 688-698.

[14] B.M. Reddy, G. Thrimurthulu, L. Katta, Y. Yamada, S.-E. Park, J. Phys. Chem. C 113 (2009) 15882-15890.

[15] D. Stošić, S. Bennici, V. Rakić, A. Auroux, Catal. Today 192 (2012) 160-168.

[16] S. Collins, G. Finos, R. Alcántara, E. del Rio, S. Bernal, A. Bonivardi, Appl. Catal. A: Gen. 388 (2010) 202-210.

[17] W. Liu, M. Flytzani-Stephanopoulos, Chem. Eng. J. 64 (1996) 283-294.

[18] Z. Chen, Z. Jiao, D. Pan, Z. Li, M. Wu, C.-H. Shek, C.M.L. Wu, J.K.L. Lai, Chem. Rev. 112 (2012) 3833-3855.

[19] S. Cimino, S. Colonna, S. De Rossi, M. Faticanti, L. Lisi, I. Pettiti, P. Porta, J. Catal. 205 (2002) 309-317.

[20] D. Delimaris, T. Ioannides, Appl. Catal. B: Environ. 84 (2008) 303-312.

[21] K. Ramesh, L. Chen, F. Chen, Y. Liu, Z. Wang, Y.-F. Han, Catal. Today 131 (2008) 477-482.

[22] Y.-F. Han, F. Chen, Z.-Y. Zhong, K. Ramesh, E. Widjaja, L.-W. Chen, Catal. Commun. 7 (2006) 739-744.

[23] J. Xu, Y.-Q. Deng, Y. Luo, W. Mao, X.-J. Yang, Y.-F. Han, J. Catal. 300 (2013) 225-234.

[24] S. Liang, F. Teng, G. Bulgan, R. Zong, Y. Zhu, J. Phys. Chem. C 112 (2008) 5307-5315.

[25] M. Abecassis-Wolfovich, M.V. Landau, A. Brenner, M. Herskowitz, Ind. Eng. Chem. Res. 43 (2004) 5089-5097.

[26] M. Casapu, O. Kröcher, M. Elsener, Appl. Catal. B: Environ. 88 (2009) 413-419.

[27] R. Jin, Y. Liu, Y. Wang, W. Cen, Z. Wu, H. Wang, X. Weng, Appl. Catal. B: Environ. 148-149 (2014) 582-588.

[28] L.E. Gómez, E.E. Miró, A.V. Boix, Int. J. Hydrogen. Energ 38 (2013) 5645-5654.

[29] S. Zeng, T. Chen, K. Liu, H. Su, Catal. Commun. 45 (2014) 16-20.

[30] D. Qiao, G. Lu, Y. Guo, Y. Wang, Y. Guo, J. Rare Earth 28 (2010) 742-746.

[31] G. Chen, F. Rosei, D. Ma, Adv. Funct. Mater. 22 (2012) 3914-3920.

[32] Z.-Q. Zou, M. Meng, Y.-Q. Zha, J. Phys. Chem. C 114 (2009) 468-477.

[33] S. Imamura, M. Shono, N. Okamoto, A. Hamada, S. Ishida, Appl. Catal. A: Gen. 142 (1996) 279-288.

[34] F. Arena, G. Trunfio, J. Negro, B. Fazio, L. Spadaro, Chem. Mater. 19 (2007) 2269-2276.

[35] J. Xu, Y.-Q. Deng, X.-M. Zhang, Y. Luo, W. Mao, X.-J. Yang, L. Ouyang, P. Tian, Y.-F. Han, ACS Catal. 4 (2014) 4106-4115.

[36] X. Wu, S. Liu, D. Weng, F. Lin, R. Ran, J. Hazard. Mater. 187 (2011) 283-290.

[37] M. Machida, M. Uto, D. Kurogi, T. Kijima, Chem. Mater. 12 (2000) 3158-3164.

[38] S.M. Lee, K.H. Park, S.C. Hong, Chem. Eng. J. 195-196 (2012) 323-331.

[39] G. Qi, R.T. Yang, J. Catal. 217 (2003) 434-441.

[40] F. Kapteijn, L. Singoredjo, A. Andreini, J.A. Moulijn, Appl. Catal. B: Environ. 3 (1994) 173-189.

[41] X. Wu, Q. Liang, D. Weng, J. Fan, R. Ran, Catal. Today 126 (2007) 430-435.

[42] X. Tang, Y. Li, X. Huang, Y. Xu, H. Zhu, J. Wang, W. Shen, Appl. Catal. B: Environ. 62 (2006) 265-273.

[43] J.-Y. Luo, M. Meng, X. Li, X.-G. Li, Y.-Q. Zha, T.-D. Hu, Y.-N. Xie, J. Zhang, J. Catal. 254 (2008) 310-324.

[44] W. Cen, Y. Liu, Z. Wu, H. Wang, X. Weng, Phys. Chem. Chem. Phys. 14 (2012)

5769-5777.

[45] D. García Pintos, A. Juan, B. Irigoyen, J. Phys. Chem. C 117 (2013) 18063-18073.

[46] A.M.T. Silva, R.R.N. Marques, R.M. Quinta-Ferreira, Appl. Catal. B: Environ. 47 (2004) 269-279.

[47] W.H. Weber, K.C. Hass, J.R. McBride, Phys. Rev. B 48 (1993) 178-185.

[48] T. Taniguchi, T. Watanabe, N. Sugiyama, A.K. Subramani, H. Wagata, N. Matsushita, M. Yoshimura, J. Phys. Chem. C 113 (2009) 19789-19793.

[49] Z.D. Dohčević-Mitrović, M.J. Šćepanović, M.U. Grujić-Brojčin, Z.V. Popović, S.B. Bošković, B.M. Matović, M.V. Zinkevich, F. Aldinger, Solid State Commun. 137 (2006) 387-390.

[50] J.R. McBride, K.C. Hass, B.D. Poindexter, W.H. Weber, J. Appl. Phys. 76 (1994) 2435-2441.

[51] F. Esch, S. Fabris, L. Zhou, T. Montini, C. Africh, P. Fornasiero, G. Comelli, R. Rosei, Science 309 (2005) 752-755.

[52] S. Rossignol, F. Gerard, D. Mesnard, C. Kappenstein, D. Duprez, J. Mater. Chem. 13 (2003) 3017-3020.

[53] C. Li, Y. Sakata, T. Arai, K. Domen, K.-i. Maruya, T. Onishi, J. Chem. Soc., Faraday Trans. 1. 85 (1989) 1451-1461.

[54] C. Li, Y. Sakata, T. Arai, K. Domen, K.-i. Maruya, T. Onishi, J. Chem. Soc., Faraday Trans. 1. 85 (1989) 929-943.

[55] E. Aneggi, M. Boaro, C.d. Leitenburg, G. Dolcetti, A. Trovarelli, J. Alloy. Compd.

408–412 (2006) 1096-1102.

[56] N. Drenchev, I. Spassova, E. Ivanova, M. Khristova, K. Hadjiivanov, Appl. Catal. B: Environ. 138-139 (2013) 362-372.

[57] F. Bozon-Verduraz, A. Bensalem, J. Chem. Soc., Faraday Trans. 90 (1994) 653-657.

[58] P. Venkataswamy, K.N. Rao, D. Jampaiah, B.M. Reddy, Appl. Catal. B: Environ. 162 (2015) 122-132.

[59] F.C. Buciuman, F. Patcas, T. Hahn, Chemical Engineering and Processing: Process Intensification 38 (1999) 563-569.

[60] F. Arena, G. Trunfio, B. Fazio, J. Negro, L. Spadaro, J. Phys. Chem. C 113 (2009) 2822-2829.

Captions

Fig. 1. XRD patterns of (A) MnO_x; (B) Mn_2Ce_1; (C) $Mn_{1.5}Ce_1$; (D) Mn_1Ce_1; (E) $Mn_{0.75}Ce_1$; (F) $Mn_{0.33}Ce_1$; (G) CeO_2.

Fig. 2. (a) TEM image and (b) HRTEM of the Mn_1Ce_1 catalyst.

Fig. 3. (a) SEM image; (b) Mn mapping image; (c) EDX element analysis; (d) Ce mapping image of the Mn_1Ce_1 catalyst.

Fig. 4. (a) Temperature-dependent CO oxidation over MnO_x-CeO_2 with different molar ratios; CO oxidation over Mn_1Ce_1 with moisture: (b) heating and cooling: 1% CO + 20% O_2 + 1.5% H_2O + 77.5% Ar; (c) heating: 1% CO + 20% O_2 + 1.5% H_2O + 77.5% Ar; cooling: 1% CO + 20% O_2 + 79% Ar.

Fig. 5. (a) The H_2-TPR profile and (b) The O_2-TPD profile of (A) MnO_x; (B) Mn_2Ce_1; (C) $Mn_{1.5}Ce_1$; (D) Mn_1Ce_1; (E) $Mn_{0.75}Ce_1$; (F) $Mn_{0.33}Ce_1$; (G) CeO_2.

Fig. 6. CO-TPR profiles of (a) pure CeO_2; (b) pure MnO_x; (c) Mn_1Ce_1 catalyst.

Fig. 7. Operando/In situ Raman spectra over CeO_2 recorded in streams of (a) Ar; (b) 1%CO (Ar balance); (c) 1%CO, 20%O_2 (Ar balance) and over Mn_1Ce_1 recorded in streams of (d) Ar; (e) 1%CO (Ar balance); (f) 1%CO, 20%O_2 (Ar balance), following the order of 25 ^oC (A), 100 ^oC (B), 200 ^oC (C), 300 ^oC (D), 400 ^oC (E), 500 ^oC (F), and back to 25 ^oC (G).

Fig. 8. In situ DRIFTS over CeO_2 at different temperatures in a flow of 1%CO/Ar (a), 1%CO and 20%O_2/Ar (b) at 25 ^oC (A), 50 ^oC (B), 100 ^oC (C), 150 ^oC (D), 200 ^oC (E), 250 ^oC (F), 300 ^oC (G), 350 ^oC (H), and 400 ^oC (I).

Fig. 9. In situ DRIFTS over MnO_x in a flow of 1%CO/Ar (a), 1%CO and 20%O_2/Ar (b), at 25 ^oC (A), 50 ^oC (B), 100 ^oC (C), 150 ^oC (D), 200 ^oC (E), 250 ^oC (F), 300 ^oC (G), 350 ^oC (H), and 400 ^oC (I).

Fig. 10. In situ DRIFTS on Mn_1Ce_1 in a flow of 1%CO/Ar (a); 1%CO + 20%O_2/Ar (b) at 25 ^oC (A), 50 ^oC (B), 100 ^oC (C), 150 ^oC (D), 200 ^oC (E), 250 ^oC (F), 300 ^oC (G), 350 ^oC (H), and 400 ^oC (I).

TABLES

Table 1. Physical structure of MnO_x-CeO_2 catalysts

Catalyst	Particle size (nm)	BET area (m^2/g)	H_2-consumption (mmol/g)	O_2-storage (mmol/g)
$Mn_{0.33}Ce_1$	10.8	77.9	0.07	0.15
$Mn_{0.75}Ce_1$	7.0	94.4	0.11	0.20
Mn_1Ce_1	<5	105.4	0.13	0.22
$Mn_{1.5}Ce_1$	<5	74.4	0.14	0.12
Mn_2Ce_1	<5	82.9	0.15	0.11
CeO_2	15.9	28.6	0.06	0.16
MnO_x	--	27.0	0.17	0.06

Table 2. Comparison of activity for CO oxidation over MnO_x-CeO_2 catalysts

Catalysts	Preparation method	Mn/Ce (molar ratio)	Reaction conditions	Activity		Refs.
				T_{10}(°C)	T_{100}(°C)	
$Ce_{0.9}Mn_{0.1}O_{2-\delta}$	Combustion	1/9	1% CO, 10% O_2 GHSV: 30000 mL/(g·h)	124	200	[30]
$MnCeO_x$	Template	1/15	1% CO, 10% O_2	-	210	[31]
Mn4Ce6	Coprecipitation	2/3	2% CO/10% O_2, SV: 30000 h^{-1}	-	125	[32]
$Ce_{0.7}Mn_{0.3}O_{2-\delta}$	Coprecipitation	3/7	CO/O_2 = 1 GHSV: 36000 mL/(g·h)	65	205	[58]
$MnCe/Al_2O_3$	Impregnation	5/2	0.5% CO, 1% O_2 GHSV: 60000 mL/(g·h)	40	250(T_{75})	[56]
MnO_x-CeO_2	Redox-coprecipitation	1/1	1% CO, 20% O_2 GHSV: 60000 mL/(g·h)	66	190	This work

Table 3. Comparison of kinetic parameters for CO oxidation over various catalysts

Catalysts	Conditions	Reaction Temperature (°C)	Reaction rate ($\mu mol_{CO}\, g^{-1}s^{-1}$)	Reaction order	Ea (kJ/mol)	Ref.
Mn_2O_3	2.5%CO, 2.5%O_2 GHSV: 36,000 h^{-1}	-	N.A.	-	57.9±2.0	[21]
α-Mn_2O_3	1%CO, 20%O_2 GHSV: 36,000 h^{-1} 100-190 °C	153	6.44	α_{CO}: 0.4→0.8 α_{O2}: 0.4→0	60.0±2.0	[23]
Mn_2O_3	2%CO, 20%O_2 GHSV: 36,000 h^{-1}	210	N.A.	α_{CO}: 0.7	61.0	[59]
Mn_3O_4@SiO_2	1%CO, 20%O_2 GHSV: 36,000 h^{-1} 200-280 °C	230	2.26	α_{CO}: 0.5→0.12 α_{O2}: 0.4~0.5	69 ± 3.0	[35]
$MnCeO_x$	2%CO, 1%O_2 GHSV: 12000 mL/(g·h)	150	14.2	α_{CO}: 0.9 α_{O2}: 0.14	62±3	[60]
Mn_1Ce_1	1% CO, 20% O_2 GHSV: 18000 h^{-1} 100-190 °C	190	7.44	α_{CO}: 0.3→0.8 α_{O2}: 0.3→0.1	29 ± 1.7	This work

FIGURES

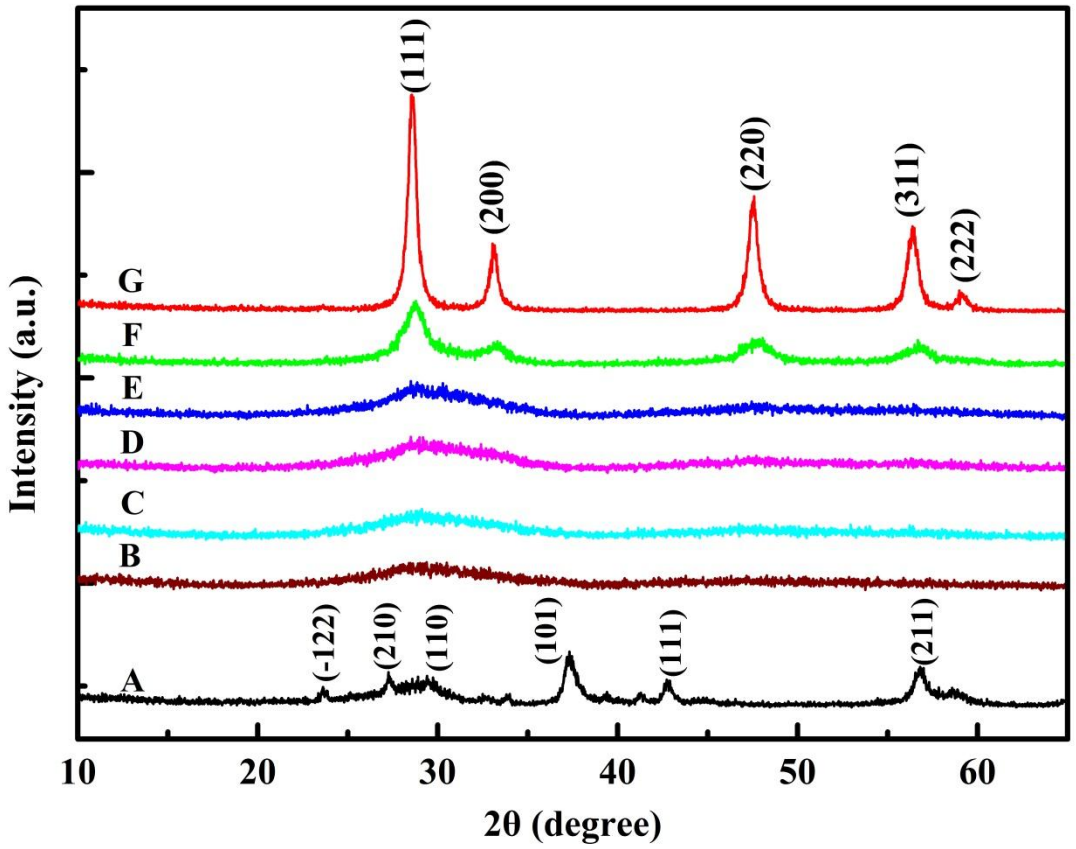

Fig. 1. XRD patterns of (A) MnO_x; (B) Mn_2Ce_1; (C) $Mn_{1.5}Ce_1$; (D) Mn_1Ce_1; (E) $Mn_{0.75}Ce_1$; (F) $Mn_{0.33}Ce_1$; (G) CeO_2.

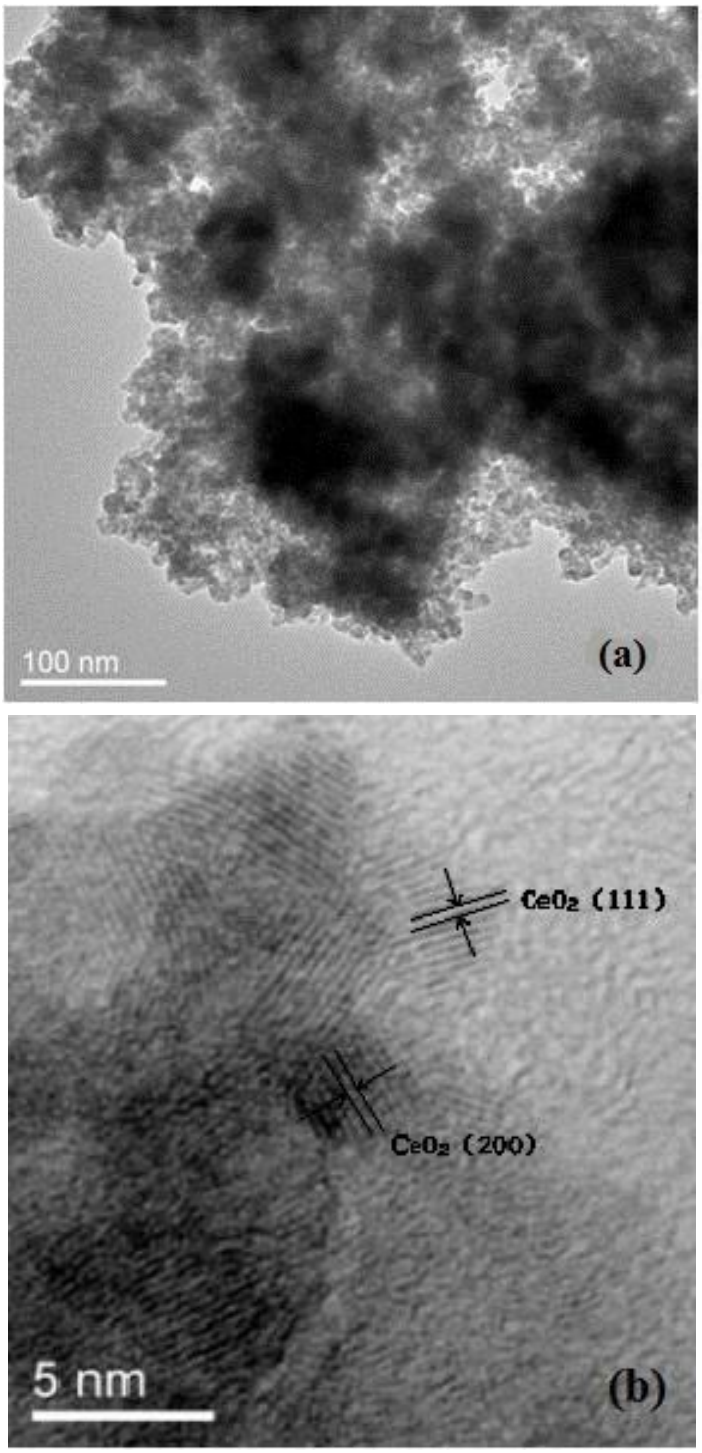

Fig. 2. (a) TEM image and (b) HRTEM of the Mn_1Ce_1 catalyst.

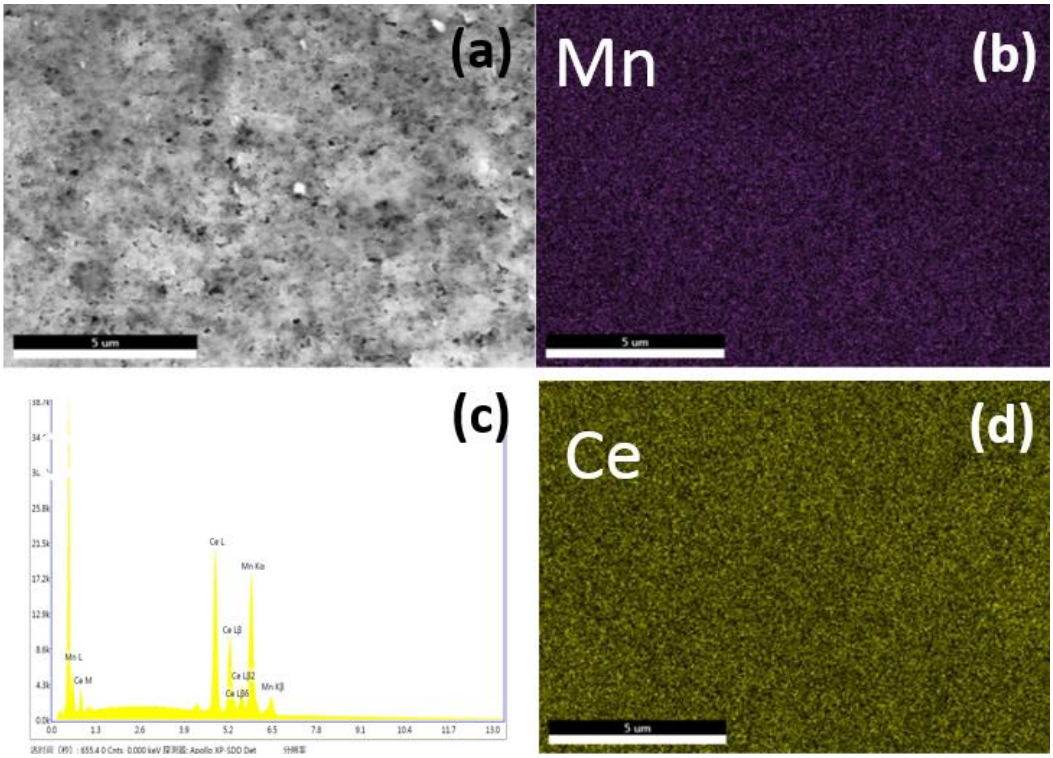

Fig. 3. (a) SEM image; (b) Mn mapping image; (c) EDX element analysis; (d) Ce mapping image of the Mn_1Ce_1 catalyst.

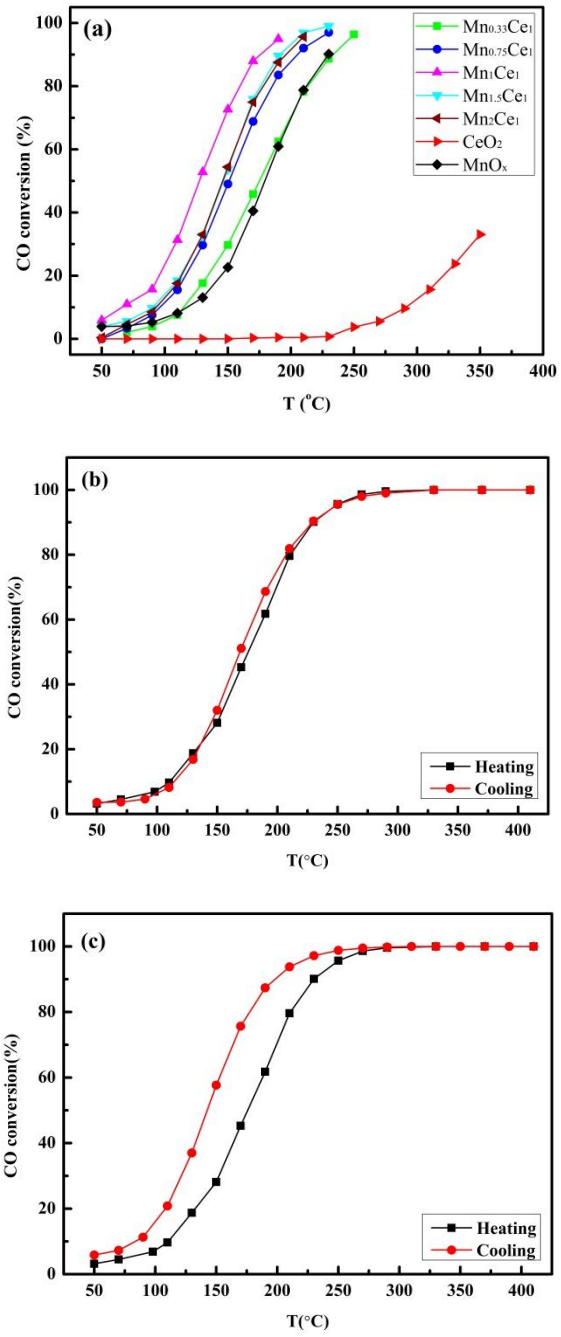

Fig. 4. (a) Temperature-dependent CO oxidation over MnO_x-CeO_2 with different molar ratios; CO oxidation over Mn_1Ce_1 with moisture: (b) heating and cooling: 1% CO + 20% O_2 + 1.5% H_2O + 77.5% Ar; (c) heating: 1% CO + 20% O_2 + 1.5% H_2O + 77.5% Ar; cooling: 1% CO + 20% O_2 + 79% Ar.

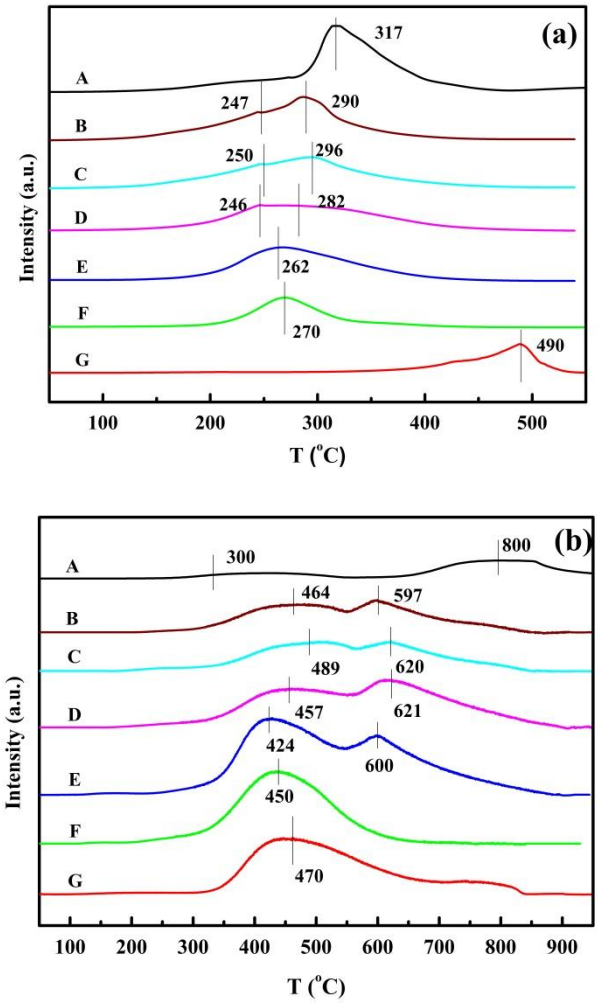

Fig. 5. (a) The H_2-TPR profile and (b) The O_2-TPD profile of (A) MnO_x; (B) Mn_2Ce_1; (C) $Mn_{1.5}Ce_1$; (D) Mn_1Ce_1; (E) $Mn_{0.75}Ce_1$; (F) $Mn_{0.33}Ce_1$; (G) CeO_2.

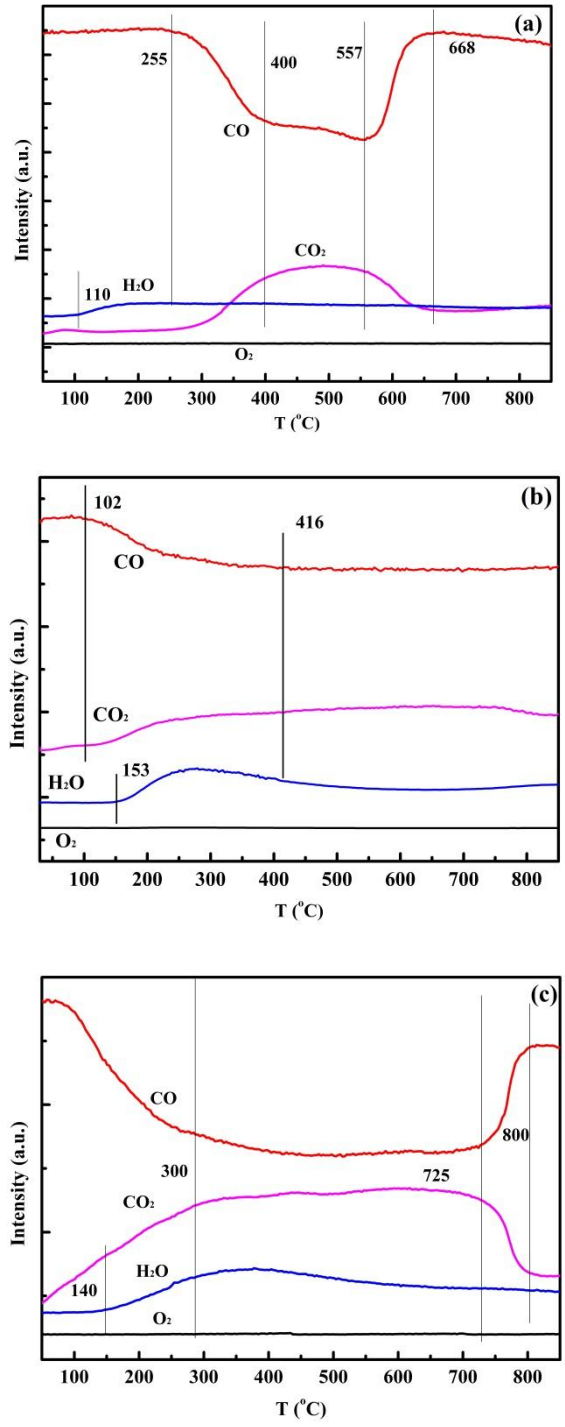

Fig. 6. CO-TPR profiles of (a) pure CeO_2; (b) pure MnO_x; (c) Mn_1Ce_1 catalyst.

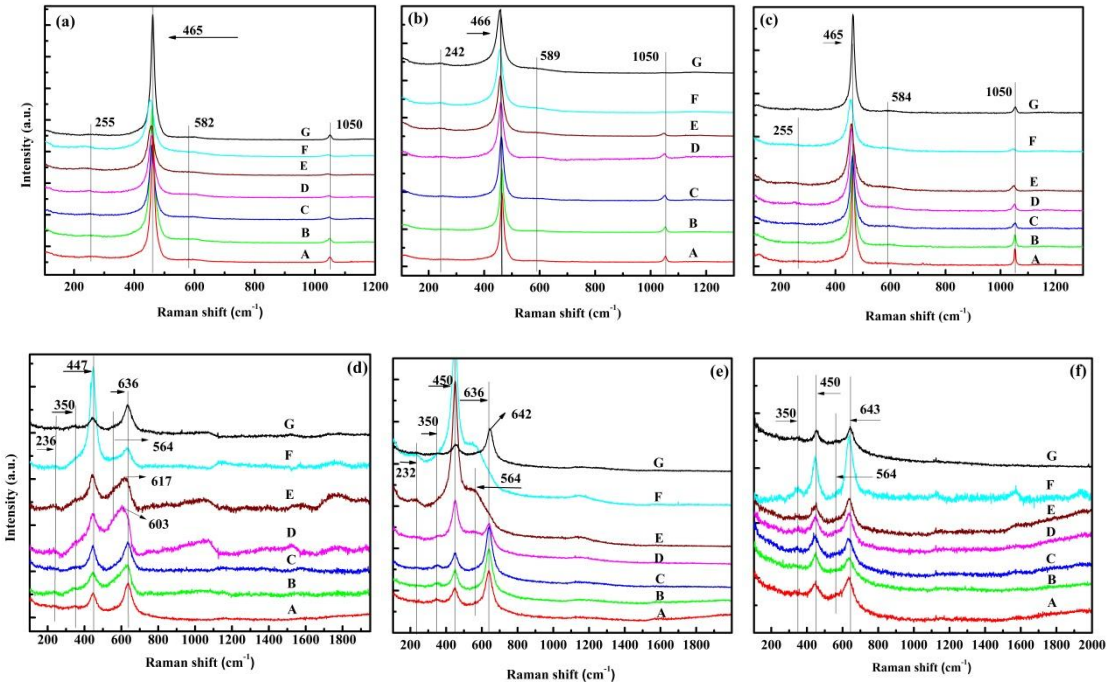

Fig. 7. Operando/In situ Raman spectra over CeO_2 recorded in streams of (a) Ar; (b) 1%CO (Ar balance); (c) 1%CO, 20%O_2 (Ar balance) and over Mn_1Ce_1 recorded in streams of (d) Ar; (e) 1%CO (Ar balance); (f) 1%CO, 20%O_2 (Ar balance), following the order of 25 ^oC (A), 100 ^oC (B), 200 ^oC (C), 300 ^oC (D), 400 ^oC (E), 500 ^oC (F), and back to 25 ^oC (G).

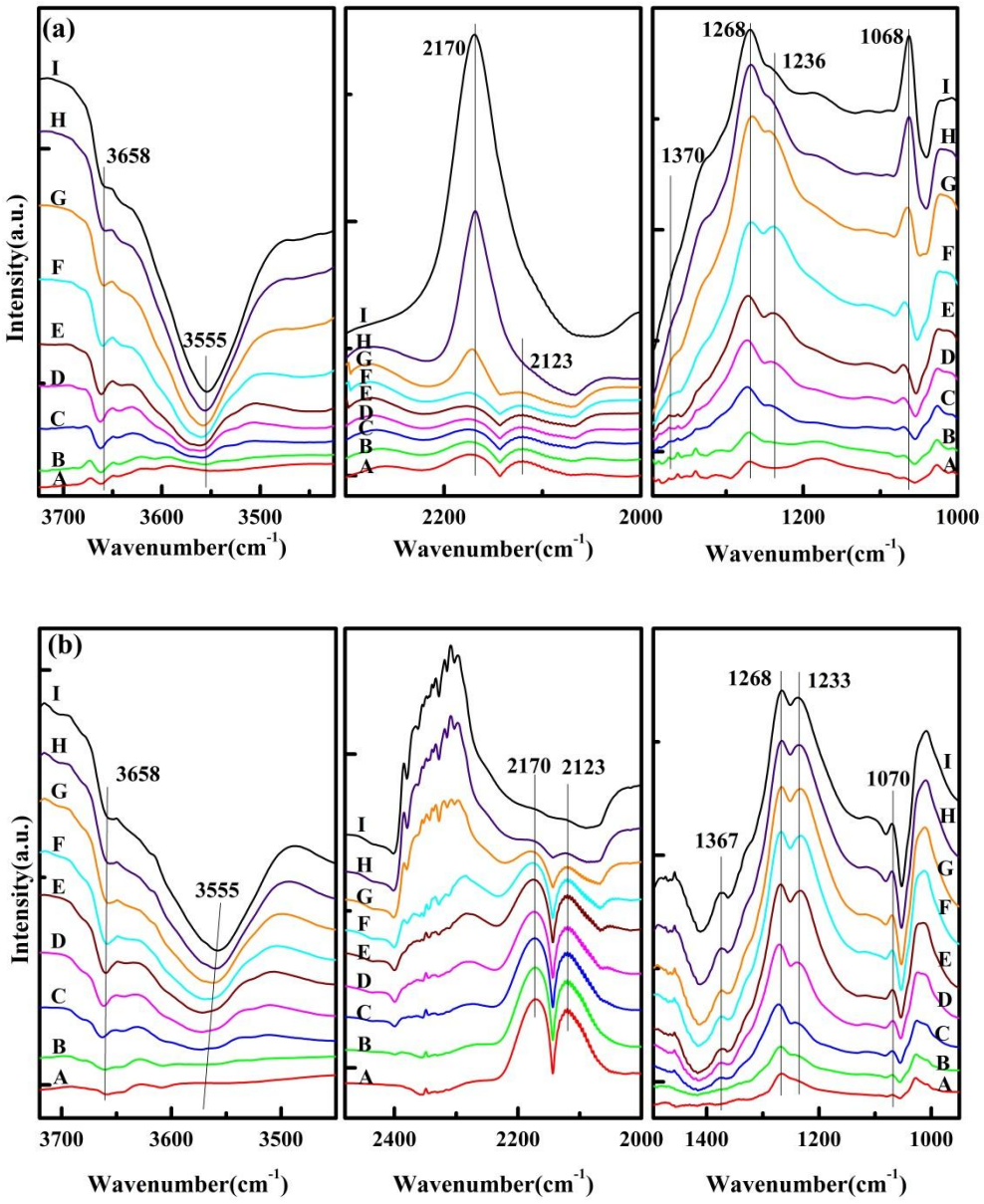

Fig. 8. In situ DRIFTS over CeO_2 at different temperatures in a flow of 1%CO/Ar (a), 1%CO and 20%O_2/Ar (b) at 25 ^{o}C (A), 50 ^{o}C (B), 100 ^{o}C (C), 150 ^{o}C (D), 200 ^{o}C (E), 250 ^{o}C (F), 300 ^{o}C (G), 350 ^{o}C (H), and 400 ^{o}C (I).

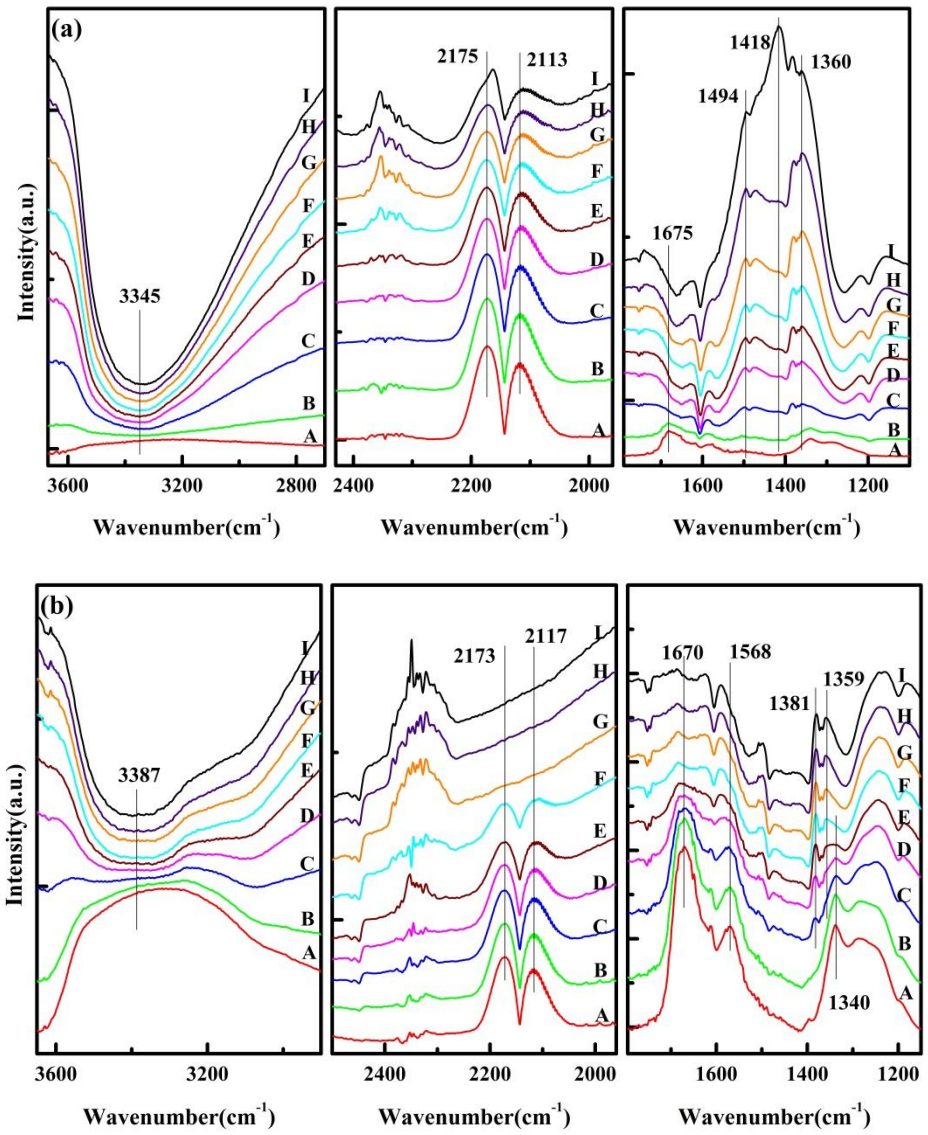

Fig. 9. In situ DRIFTS over MnO_x in a flow of 1%CO/Ar (a), 1%CO and 20%O_2/Ar (b), at 25 ^oC (A), 50 ^oC (B), 100 ^oC (C), 150 ^oC (D), 200 ^oC (E), 250 ^oC (F), 300 ^oC (G), 350 ^oC (H), and 400 ^oC (I).

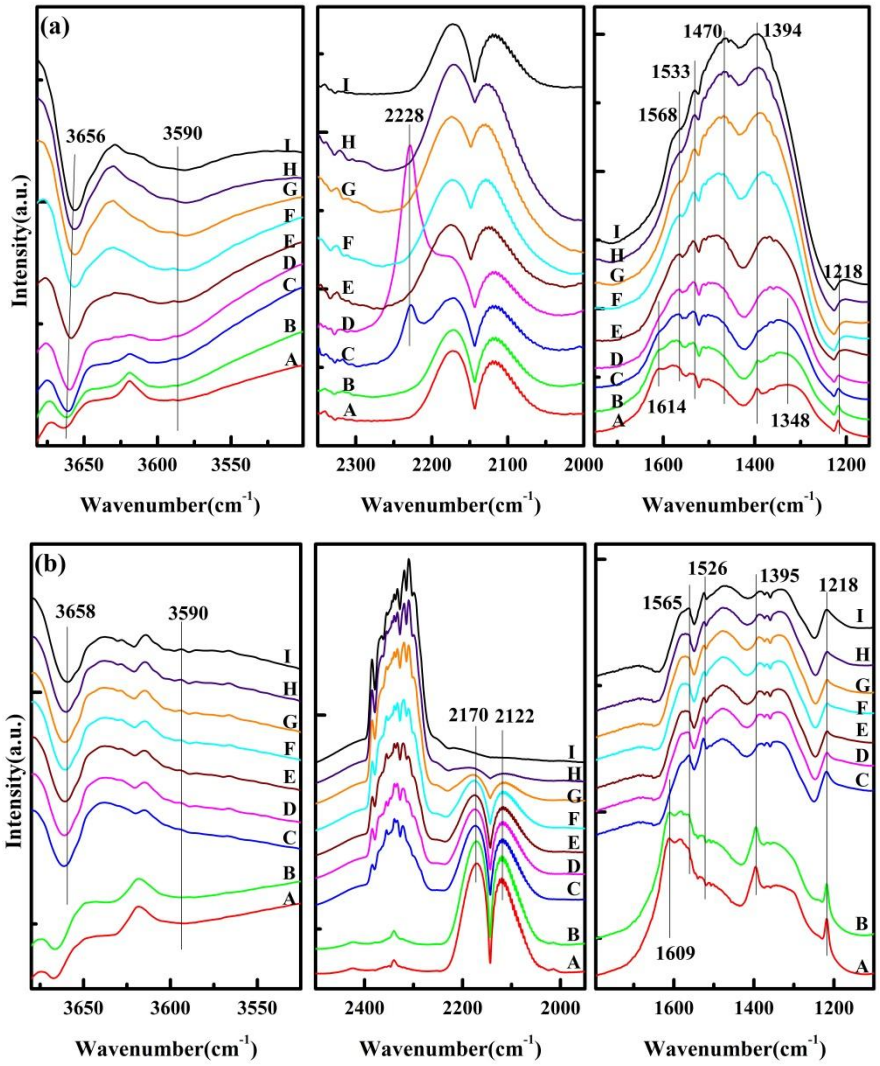

Fig. 10. In situ DRIFTS on Mn_1Ce_1 in a flow of 1%CO/Ar (a); 1%CO + 20%O_2/Ar (b) at 25 ^oC (A), 50 ^oC (B), 100 ^oC (C), 150 ^oC (D), 200 ^oC (E), 250 ^oC (F), 300 ^oC (G), 350 ^oC (H), and 400 ^oC (I).

Graphical abstract